

Polar Wind Survey with TIDE/PSI Suite Aboard POLAR

Yi-Jiun Su and J. L. Horwitz

Center for Space Plasma and Aeromonic Research, The University of Alabama in Huntsville,
Huntsville, Alabama

T. E. Moore and B. L. Giles

Laboratory for Extraterrestrial Physics, Goddard Space Flight Center, Greenbelt, Maryland

M. O. Chandler and P. D. Craven

Space Sciences Laboratory, Marshall Space Flight Center, Huntsville, Alabama

M. Hirahara

Department of Physics, Rikkyo University, Tokyo, Japan

C. J. Pollock

Instrumentation and Space Research Division, Southwest Research Institute, San Antonio, Texas

Short title: POLAR WIND SURVEY

Abstract. In February, 1996, the POLAR spacecraft was placed in a 90 degree inclination, elliptical orbit with a $9 R_E$ geocentric distance apogee in the northern hemisphere and $1.8 R_E$ geocentric distance perigee in the southern hemisphere. The Thermal Ion Dynamics Experiment (TIDE) on POLAR has allowed sampling of the three-dimensional ion distribution functions with excellent energy, angular, and mass resolution. The Plasma Source Instrument (PSI), when operated, allows sufficient diminution of the electric potential to observe the polar wind at very high altitudes. In this paper, we describe the results of a survey of the polar wind characteristics for H^+ , He^+ , and O^+ as observed by TIDE at low (~ 5000 km) and high ($\sim 8 R_E$) altitudes over the polar cap during April – May, 1996. At 5000 km altitude, the H^+ polar wind exhibits a supersonic outflow, while O^+ shows subsonic downflow, which suggests a cleft ion fountain origin for the O^+ ions in the polar cap region. O^+ is the dominant ion species at 5000 km. At $8 R_E$ altitude, both H^+ and O^+ are supersonic outflows, and H^+ is the highly dominant ion species. The ion perpendicular temperature is higher than the parallel temperature at low altitudes while the parallel temperature is higher at high altitudes. Dramatic decreases of the 5000 km altitude H^+ and O^+ ion densities and fluxes are seen from 90° to 100° solar zenith angle for the ionospheric base, which is consistent with solar illumination ionization control of the 5000 km ion densities. However, the polar cap downward O^+ flow and density decline from dayside to nightside suggesting a cleft ion fountain origin for the polar cap O^+ at 5000 km altitude. Cleft-ion-fountain origin O^+ density plumes could also be partially responsible for a similar day-night asymmetry in H^+ , due to the charge-exchange reaction, $O^+ + H \rightarrow H^+ + O$. At high altitude, the typical velocity ratios, $V_{O^+} : V_{He^+} : V_{H^+} \sim 2 : 3 : 5$, may suggest the importance of comparable energy gains, such as via an electric potential layer produced, for example by photoelectron effects. The survey results to date are consistent with the concept derived from Dynamics Explorer (DE) 1 of a "fountain in a wind" of O^+ and more energetic light ions emanating from the dayside auroral oval, while also exhibiting H^+ characteristics which are reasonably consistent with theoretical descriptions of a thermal polar wind, independent of any auroral energy inputs. The survey clearly indicates new directions for future polar wind modeling studies, which should account for the closed circulation of polar plasma

tubes with auroral energy inputs upon passage through the dayside and nightside auroral zones.

1. Introduction

The polar wind is an ambipolar outflow of thermal plasma from the terrestrial ionosphere at high latitude to the magnetosphere along geomagnetic field lines, consisting mainly of H^+ , O^+ , and He^+ ions and electrons. Understanding the characteristics of the polar wind is important for many reasons. For example, the ionosphere serves as a primary source of magnetospheric plasma [Horwitz, 1982, 1987, 1995; Shelley *et al.*, 1982; Moore *et al.*, 1986a, b; Chappell *et al.*, 1987; Moore and Delcourt, 1995; Ganguli, 1996; Horwitz and Moore, 1997], and the polar wind is a principal means by which the ionospheric plasma is transported to the magnetosphere. Various characteristics of the polar wind have been modeled using hydrodynamic, generalized transport, kinetic, semikinetiic, hybrid, and time-dependent approaches [e.g., Banks and Holzer, 1969; Dessler and Cloutier, 1969; Raitt *et al.*, 1975; Schunk and Watkins, 1981, 1982; Horwitz and Lockwood, 1985; Gombosi *et al.*, 1985; Ganguli *et al.*, 1987; Gombosi and Schunk, 1988; Swift, 1990; Wilson *et al.*, 1990; Wilson, 1992; Demars and Schunk, 1994; Horwitz *et al.*, 1994; Tam *et al.*, 1995; Schunk and Sojka, 1997; Demars *et al.*, 1998; Su *et al.*, 1998].

Direct observations of the polar wind were first made by Explorer 31 for the altitude range 500 to 3000 km [Hoffman, 1970; Brinton *et al.*, 1971; Hoffman *et al.*, 1974]. These data showed H^+ ion flow velocities of up to 10 km s^{-1} parallel to the geomagnetic field and outward flux levels of the order of $10^8 \text{ cm}^{-2} \text{ s}^{-1}$ above 2500 km. Polar wind observations from ISIS 2 (in a circular polar orbit at 1400 km) [Hoffman and Dodson, 1980] confirmed that an upward flow of both H^+ and He^+ ions exists over the polar cap. H^+ fluxes between 10^7 and $10^8 \text{ cm}^{-2} \text{ s}^{-1}$ were observed, and O^+ was found to be the dominant ion species at 1400 km altitude, where strong H^+ flows occur. H^+ flows along high latitude field lines showing supersonic characteristics (the Mach number ranged from 2.6 to 5.1) at $2 R_E$ were observed for the first time by the Retarding Ion Mass Spectrometer (RIMS) on Dynamics Explorer (DE) 1 [Nagai *et al.*, 1984; Olsen *et al.*, 1986], in general accord with classical polar wind model results. Observed H^+ flux values mapped to 1000 km were about $2.6 \times 10^8 \text{ cm}^{-2} \text{ s}^{-1}$ for disturbed conditions ($Kp = 5-$).

High altitude observations by the DE 1/High Altitude Plasma Instrument (HAPI) over polar regions indicated that the polar outflow consists of two ion components [*Gurgiolo and Burch, 1982*]. One unheated component is the “classical” polar wind; the other component involves perpendicular ion heating over the cusp and possibly in the polar cap. The altitude at which the heating occurred was estimated to lie between 8000 and 12,000 km. In addition to the classical polar wind, *Shelley et al.* [1982] have reported the existence of O^+ -dominated upward flowing ion events (with about 10% H^+) over the polar cap in the energy range from 0 to 100 eV above the spacecraft potential using DE 1/Energetic Ion Composition Spectrometer (EICS), and further estimated that these ion outflow fluxes with an order of $10^6 \text{ cm}^{-2} \text{ s}^{-1}$ at $4.6 R_E$ (DE 1 apogee) were most likely the source of the tail lobe ion streams. A statistical study using DE 1/EICS data [*Yau et al., 1984*] confirmed the importance of low energy outflow of O^+ over the high altitude polar cap.

Waite et al. [1985] have reported several distinguishing characteristics of O^+ outflows from DE 1 observations between October 7 and November 26, 1981. The low-energy O^+ outflow (2 to 10 eV) was a long-duration outflow at high altitudes over most of the polar cap during active magnetic conditions. The field-aligned distribution had a low temperature, 2000 to 5000 K, a fairly large drift velocity of 5 to 15 km s^{-1} , and a large flux ranging from 10^6 to $10^7 \text{ cm}^{-2} \text{ s}^{-1}$, corresponding to about 5×10^7 to $5 \times 10^8 \text{ cm}^{-2} \text{ s}^{-1}$ mapped downward along the diverging magnetic field to the ionosphere. The observations of *Waite et al.* [1985] also pointed to the cleft region as a source of O^+ to the high-altitude polar cap. It was noted that the cleft or cusp represents a strong source of upflowing ions, particularly O^+ , over the polar cap region [*Lockwood et al., 1985a, b*]. With low-energy ion measurements (RIMS) on DE 1 satellite, *Lockwood et al.* [1985b] concluded that upwelling ions at the cleft form an ion fountain and are blown into the polar cap by antisunward convection. The transport of ionospheric ions from a source in the polar cleft ionosphere through the polar magnetosphere was investigated using a two-dimensional, kinetic, trajectory-based code by *Horwitz and Lockwood* [1985]. Their resulting plasma distributions and parameters are in general agreement with low-energy ion measurements (RIMS) [*Lockwood et al., 1985b*]. *Pollock et al.* [1990]

found that the upwelling plasma below $3 R_E$ is rich in O^+ , which typically comprises about 90% of the ion density in the dayside cleft region for spring conditions during an active portion of the solar cycle. The typical upwelling O^+ ion flux from *Pollock et al.* [1990] was about $6 \times 10^8 \text{ cm}^{-2} \text{ s}^{-1}$ (mapped to an altitude of 1000 km). There is, however, no clear-cut relationship between either the occurrence or intensity of upwelling ion events and the immediately preceding hourly averaged value of the IMF B_z component.

Observations of H^+ , He^+ , and O^+ with energies down to spacecraft potential were reported by *Chandler et al.* [1991], whose data set encompassed the period from autumn 1981 through 1983 between the altitude of 1000 to 4000 km at invariant latitudes greater than 70° . They showed that the average density of each ion species decreases with altitude. In the altitude range 1000 to 4000 km, O^+ is always the dominant ion (10^3 cm^{-3}), with an H^+ density of about 100 cm^{-3} and He^+ density of around 10 cm^{-3} . The H^+ velocity increased from 4 to 10 km s^{-1} over the altitude range 1000 to 4000 km. Observations of the H^+ , He^+ , and O^+ polar wind ions in the polar cap ($> 80^\circ$ invariant latitude, ILT) from 2000 to 10,000 km altitude from Akebono were reported by *Abe et al.* [1993a, b]: both the ion parallel velocity and temperature distributions exhibited a day-to-night asymmetry, showing higher average values of parallel velocities and temperatures on the dayside than on the nightside. For all three ion species, the parallel ion velocity increased with altitude. The average H^+ velocity reached 1 km s^{-1} near 2000 km, as did the He^+ velocity near 3000 km and the O^+ velocity near 6000 km. At Akebono apogee (10,000 km), the average H^+ , He^+ and O^+ velocities were near 12, 7, and 4 km s^{-1} , respectively. DE 1/RIMS observations of O^+ velocities by *Chandler* [1995] showed both upward and downward O^+ flows at DE 1 apogee: the upflows occurred in the dayside cusp region and at auroral latitudes during all local times, while the downflows were restricted to the polar cap. Global ionosphere-polar wind simulations by *Schunk and Sojka* [1997] presented similar results. The O^+ velocity field observed by *Chandler* [1991] is consistent with a scenario which has O^+ of cusp/cleft and auroral zone origin convected into the polar cap and, because of the dominance of gravitational energy over the upward kinetic energy, falling back into the polar cap ionosphere [e.g., *Horwitz and Lockwood*, 1985].

The POLAR spacecraft was launched on February 24, 1996 into a 90° inclination, polar elliptical orbit with $9 R_E$ apogee geocentric distance in the northern hemisphere and $1.8 R_E$ perigee in the southern hemisphere [Acuña *et al.*, 1995]. The Thermal Ion Dynamics Experiment (TIDE) on POLAR samples the three-dimensional ion distributions once per 6 second spin of the spacecraft with excellent low energy, angular (22.5° polar angle resolution and 11.25° spin azimuth resolution), and mass resolution for the 0.3 – 450 eV energy range [Moore *et al.*, 1995]. The accompanying Plasma Source Instrument (PSI), when operated, allows sufficient diminution of the electric potential to observe the low-energy polar wind ions at very high altitudes [Moore *et al.*, 1997].

This paper presents a survey of the polar wind characteristics in the polar cap region near 5000 km altitude (perigee) in the southern hemisphere and $8 R_E$ altitude (apogee) in the northern hemisphere. The apogee measurements included in the paper were during the early portion (April–May) of the POLAR mission in 1996 when PSI was operating. We do not include data collected from June through July 1996 due to unreliable calibrations during these periods. Beginning with August 1996, the TIDE time-of-flight (TOF) mass analyzer stopped functioning properly and could not distinguish the different ion species. In our survey, each sample is based on data accumulated over one minute (10 spins).

A special analysis technique for ion bulk parameter estimates is described in the following section. Using this technique for the parameters, the general bulk parameter trends and averages for the 5000 km polar wind are presented in the section 3. The relationships of ion bulk parameters with the solar zenith angle and with the day-night distance in the solar magnetic coordinate system at 5000 km altitude are also presented in the section 3. In section 4, we show the polar wind characteristics and general trends in bulk parameters for POLAR apogee when PSI was operating. We summarize and discuss our polar wind survey in section 5.

2. Ion Bulk Parameter Analysis

In this paper, we only focus on the “quiet” polar wind, excluding the cusp/cleft region and auroral zone, which are distinguishable in the ion “chromograms”. A typical example at POLAR perigee is shown in Figure 1. In Figure 1, the spacecraft passes through the auroral zone (03:22:00 – 03:27:00 UT), polar cap (03:27:00 – 03:42:00 UT), and cusp/cleft region (03:42:00 – 03:49:00 UT) on April 4, 1996. Our study here is restricted to low energy ions (less than 10 V, seen as red in this figure), i.e., the polar wind, in the polar cap region, and excludes data from the cusp/cleft and auroral regions. The H^+ ion flow peaks between the magnetic field line direction (“+” signs) and the ram direction (“×” signs) in the top panel, while O^+ ions flow primarily along the ram direction in the bottom panel. The additional counts seen between the magnetic field line and ram directions in the bottom panel are spurious signals resulting from H^+ ion counts in the O^+ channel, “ghost peaks”, and are excluded in our analysis.

TIDE was designed to measure very low energy ions and was tested and calibrated with laboratory beams having energies down to 0.6 eV. However, the very lowest energy portion of the low energy ion distributions, even at 5000 km altitude, is still shielded from the spacecraft (the spacecraft potential is usually ≥ 1.8 V). Typical O^+ and H^+ phase space density distributions at perigee are shown in Figures 2 (a) and (b) from 03:34:57 to 03:35:36 UT (one minute average) on April 23, 1996, in which the x axis is defined by the local magnetic field, the y axis is defined by the normal vector lying in the spacecraft orbit plane, and the z axis is orthogonal to the x and y axis. In the left panel of Figure 2 (a), the phase spaced density distribution is sliced in the plane perpendicular to the local magnetic field for an O^+ velocity of $V_x = -1.1 \text{ km s}^{-1}$. The right panel shows a slice in the parallel plane with $V_z = -0.8 \text{ km s}^{-1}$. Likewise, a perpendicular plane of H^+ distribution with $V_x = 15.8 \text{ km s}^{-1}$ is seen in the left panel of Figure 2 (b) while the right panel shows a parallel plane with $V_z = -4.5 \text{ km s}^{-1}$. We note that the polar wind moments are only calculated by the restricted region in energy, spin azimuth, and polar angle as indicated on the plots. Only a relatively small region of velocity space (approximately the region of $V_x = [-8, 12]$, $V_y = [-10, 10]$, and $V_z = [-15, 10] \text{ km/s}$ in Figure 2a, and the region of $V_x = [-12, 35]$, $V_y = [-20, 20]$, and $V_z = [-22, 25] \text{ km/s}$

in Figure 2b) has been calculated, so that the outlying velocity space region do not contributed to the moments. The “standard” moments calculation does not include contributions from portions of the distributions reflected by the spacecraft potential (1.73 V for the case in Figure 2). This shielding is especially severe for H^+ ions, i.e. the crescent shaped partial distribution in the right panel of Figure 2 (b). Therefore, we use an iterative bi-Maxwellian “filling” technique to fill in the 3-dimensional distributions in order to obtain the improved bulk parameter estimates (described below). In addition, we have corrected for an anomalous enhancement in the low energy channels (Retarding Potential Analyzer (RPA) channels < 4 eV) for the polar sector 4 ($57.5^\circ - 90^\circ$). We therefore substitute the average of measurements (for perigee only) from polar sectors 3 and 5 for those of (the abnormally high sensitivity) sector 4 before the distribution filling-in process for our study. Only 12 of the 31 energy bins for sector 4 were adjusted by this method.

The basic analysis approach with our filling-in procedure proceeded as follows: first, we localized our region of distribution function analysis in energy, spin azimuth, and polar angle to obtain a generally narrow ion beam, consisting only of the low-energy polar wind stream, among other reasons in order to exclude “ghost peaks” (spurious signals resulting from other ion species) and “sun pulses” (spurious counts associated with sunlight leaks) when calculating the moments. The original density, velocity, and temperature from the “standard” TIDE moments calculation are assumed as the initial input parameters to drive the iterative filling procedure. Using these initial moments, a drifting bi-Maxwellian distribution is generated and used to fill in the portion of the distribution which is shielded by the spacecraft potential. The drifting bi-Maxwellian is of the form :

$$f = N \left(\frac{m}{2\pi k T_{\parallel}} \right)^{\frac{1}{2}} \left(\frac{m}{2\pi k T_{\perp}} \right) \exp \left\{ -\frac{m(V_x - V_{x_0})^2}{2kT_{\parallel}} - \frac{m[(V_y - V_{y_0})^2 + (V_z - V_{z_0})^2]}{2kT_{\perp}} \right\} \quad (1)$$

where m , k , N , T_{\parallel} , and T_{\perp} are the ion mass, Boltzmann constant, density, and parallel and perpendicular temperatures, respectively. V_x , V_y , and V_z are the parallel velocity and two components of perpendicular velocities, where the x axis is the parallel magnetic field direction, the y axis is the normal direction lying

in the spacecraft orbit plane, and the z axis is orthogonal to x and y axis. V_o indicates the bulk flow velocity. N , V_{Xo} , V_{Yo} , V_{Zo} , $T_{||}$, and T_{\perp} are supplied by the initial (or previous) moment calculation.

The new moments are calculated from the original distribution (f_i) for outside the shielded region and from the generated bi-Maxwellian distribution function for the originally shielded region. We then iterate this process until it converges, attaining a minimum deviation, $|f_i - f_{biM}(\Phi > \Phi_{sc})|_{\text{minimum}}$, or when the parameters remain stable under successive iterations. In this way, the actual measurements are always honored (outside the shielded region) while using them as the basis for estimating the “most likely” values for the region of velocity space that are obscured by the spacecraft potential. This special iterative filling-in procedure is summarized in the flowchart as shown in Figure 3.

At POLAR perigee, it is often found that more than 50% of the H^+ distribution appears to be shielded by the spacecraft potential. Reasonable initial input estimates are required; otherwise, the filling-in process will not converge. We first used the process described above to fill in the O^+ distribution assuming that O^+ and H^+ have the same convection velocity. The resulting O^+ convection velocity is then assumed as the initial input convection velocity for H^+ distribution. To begin the iteration for the H^+ distribution moments, we used the higher density and temperatures from the original moments calculation as the initial input parameters. After the iterative filling process, significantly more accurate ion densities, velocities, and temperatures are obtained. For O^+ distributions, the number of iterations is usually 2 or 3 until it reaches the minimum deviation. For H^+ distributions, the number of iterations, however, depends sensitively on the initial input estimates of density and temperatures which may be near or far from the final estimates. The iterative filling process improved the TIDE bulk parameter estimates, in particular the H^+ and O^+ convection velocities that are in better agreement with each other.

Figure 4 shows the H^+ distribution after completing the filling process in both the parallel (right panel) and perpendicular planes (left panel) from 03:34:57 to 03:35:56 UT on April 23, 1996, starting from the original distribution shown in Figure 2 (b). Both density and temperature of the H^+ ions are seen to increase relative to the unmodified moments after the filling process, while the parallel velocity is seen to

decrease. For example, the original density, parallel and perpendicular temperatures, and velocities in x, y, and z components for the H^+ ion distribution are 4.8 cm^{-3} , 0.13 and 0.22 eV, and 15.8, -4.16 , and -4.48 km s^{-1} , respectively, in Figure 2 (b). After the “filling” process, the new density, parallel and perpendicular temperatures, and velocities in x, y, and z components are 9.77 cm^{-3} , 0.15 and 0.24 eV, and 12.1, 0.23, and -0.008 km s^{-1} as seen in Figure 4.

Figure 5 shows typical O^+ (open symbols) and H^+ (solid symbols) polar wind bulk parameters for one perigee pass from 05:13:35 to 05:26:05 UT on April 20, 1996, based on the moments using the “filling” analysis. O^+ parameters are represented by the open symbols, while H^+ parameters are represented by the closed symbols. The O^+ density and temperature are larger than the H^+ density and temperature, in general. O^+ and H^+ convection velocities (square and triangle symbols in the middle panel) generally tend to coincide when the H^+ densities are greater than 1 cm^{-3} , such as for the example in Figure 5. The polar wind characteristics at 5000 km altitude are discussed in the following section.

There are several origins of possible uncertainties in the presented parameters: (1) The Poisson statistics error estimation associated with the individual measurements (See the appendix in *Moore et al.* [1996]); (2) The uncertainties due to using the average of the polar sectors 3 and 5 replacing sector 4 for the low energy channels, which would become important if the distribution were a narrow beam centered on sector 4; (3) The uncertainties due to using the assumed bi-Maxwellian distribution to fill in the shielded region of velocity space; (4) The uncertainties associated with absolute calibration. For example, we may need to compare the densities measured by TIDE with possible density measurements by the Plasma Wave Instrument (PWI) [*Gurnett et al.*, 1995] to re-calibrate the countrate-flux conversion for the TIDE instruments. (5) The uncertainties due to geophysics fluctuations during the one minute accumulation intervals. However, we believe that the polar wind characteristics described in this paper should be representative of the real polar wind attributes.

We do not have quantitative estimates for all the possible uncertainties by this time. Some of these uncertainties require further investigation. Here, we only estimate the Poisson statistics based errors

associated with the individual measurements based on the appendix in *Moore et al.* [1996]. The fractional error in the density moments owing to counting statistics is approximately equal to the fractional error of the highest phase space density in the distribution (\sqrt{n}/n , where n is the ion counts). For a typical POLAR perigee on April 23, 1996, the O^+ peak count samples were ≤ 1235 counts, so the uncertainty percentage above was approximately 2.85%. The H^+ peak count samples were ≤ 140 counts, so the uncertainty percentage is estimated as approximately 8.45%.

3. Survey of the 5000 km Altitude Polar Wind

The TIDE observations at POLAR perigee (about 5000 km altitude) reported here were made over the southern polar cap. Excluding the cleft/cusp and auroral regions, we analyzed 20 perigee orbits of TIDE data in April, 1996. Each sample data is averaged over one minute. The moments calculations for the ion densities, velocities, and temperatures were based on the iterative “filling” techniques described in the last section. First, we discuss the relationship of the obtained polar wind parameters with solar zenith angle (SZA), and then present polar wind characteristics and general trends in the obtained bulk parameters. We finally discuss the relationship of the bulk parameters with day-night distance in the solar magnetic (SM) coordinate system.

3.1 Relationship of Parameters at 5000 km Altitude with Solar Zenith Angle

Measurements from 5000 to 10,000 km altitude by the Akebono satellite have indicated higher polar wind velocities in the sunlit region than on the nightside [*Abe et al.*, 1993a]. Recent simulation results of the photoelectron-driven polar wind [*Su et al.*, 1998] have shown a dramatic decrease in the photoelectron number flux at 800 km altitude as the solar zenith angle increases from about 90° to 105° , which is shown on the top in Figure 6. Using the same coupled fluid-semikinetic model, a plot of the O^+ density versus the solar zenith angle is shown at the bottom in Figure 6 at 500 km altitude, which shows the O^+ densities decreasing with increasing solar zenith angle also. These could suggest strong solar illumination ionization

control of topside ionosphere densities in the polar cap. We therefore sought to relate polar wind characteristics from TIDE observations to the solar zenith angle.

Plots of the H^+ and O^+ densities, H^+ and O^+ parallel velocities, O^+/H^+ density ratio, and H^+ and O^+ number fluxes from TIDE versus solar zenith angle are shown in Figures 7 (a) – 7 (g), respectively. In the panel (g), O^+ number fluxes versus SZA included the upward (the top panel with the range from 10^3 to 10^7 $\text{cm}^{-2} \text{ s}^{-1}$) and downward fluxes (the bottom panel with the range from -10^7 to -10^3 $\text{cm}^{-2} \text{ s}^{-1}$) and the triangle symbols represent the averages from both upward and downward fluxes at 5 degree intervals in SZA. It is interesting to note that the H^+ (a) and O^+ densities (b) and O^+ number fluxes (g) decrease dramatically with increasing SZA in the range 90° to 105° . The straight lines in (a) and (b) are the linear least-square fits for ion densities in log scale. The high correlation coefficients with SZA, $r = 0.93$ for H^+ density and $r = 0.95$ for O^+ density, may suggest the polar wind is strongly controlled by the solar illumination of the base ionosphere. When the ion density was lower than 0.1 cm^{-3} at perigee (typically the case for H^+ at $\text{SZA} > 100^\circ$), the polar wind signature was seen neither in the chromograms nor in the phase space density velocity distributions, because densities were very low or because the energies were lower than the spacecraft potential ($3 - 5 \text{ V}$ at those cases) or for both reasons. Therefore, we do not include data in which the density estimate was less than 0.1 cm^{-3} in our study of polar wind characteristics. That is why the H^+ velocity and number flux profiles are not displayed beyond 100° SZA in Figures 7 (c) and (f). The negative (downward) O^+ velocities and O^+ number fluxes are seen in (d) and (g) for low and high SZA in general. The O^+/H^+ density ratios (e) increase with increasing SZA, but again there is an uncertainty for H^+ parameters when the SZA is greater than 100° . We do not include the polar wind perigee data after April, 1996, in our survey, because the spacecraft potential was usually higher than 3 V at POLAR perigee. Hence, only O^+ polar wind was seen after April, 1996, at POLAR perigee.

3.2 General Bulk Parameter Trends and Averages for the 5000 km Polar Wind

The polar wind as observed by POLAR/TIDE at 5000 km altitude has several distinguishing characteristics. Occurrence histograms for H^+ bulk parameters are shown in Figure 8, including density

(top-left panel), parallel velocity (middle-left panel), parallel number flux (bottom-left panel), parallel temperature (top-right panel), and perpendicular temperature histograms (middle-right panel). Most of the data were sampled for the lower SZA ($\leq 100^\circ$) regions when the H^+ density was greater than our threshold density, 0.1 cm^{-3} . The H^+ densities at 5000 km range from 0.1 to 100 cm^{-3} , the H^+ parallel velocities range from 10 to 21 km s^{-1} , the H^+ parallel number fluxes range from 10^5 to $10^8 \text{ cm}^{-2} \text{ s}^{-1}$, and the parallel and perpendicular temperatures range from 0.05 to 0.45 eV . The average H^+ density, parallel velocity, number flux, parallel temperature, and perpendicular temperature are about 10 cm^{-3} , 15 km s^{-1} , $1.2 \times 10^7 \text{ cm}^{-2} \text{ s}^{-1}$, 0.12 eV ($\sim 1390 \text{ K}$), and 0.23 eV ($\sim 2670 \text{ K}$), respectively.

Occurrence plots for O^+ bulk parameters are shown in Figure 9, including density (top-left panel), parallel velocity (middle-left panel), parallel downward and upward number flux (bottom-left and bottom-right panels), parallel temperature (top-right panel), and perpendicular temperature histograms (middle-right panel). The lines with solid circles are summed from a total of 20 POLAR perigee passes with the average value displayed by the vertical solid line. The lines with open circles are for the low SZA ($\leq 100^\circ$) passes only with the average shown as the vertical dashed line. The O^+ densities range from 0.1 to 100 cm^{-3} , the velocities range from -3 to 2 km s^{-1} , the downward and upward parallel number fluxes range from 10^4 to $10^7 \text{ cm}^{-2} \text{ s}^{-1}$, and the parallel and perpendicular temperatures range from 0.2 to 1.4 eV . We have observed mostly downward O^+ flows at 5000 km altitude in the polar cap, which is consistent with the DE 1 observations in the polar cap by *Chandler* [1995]. This may provide additional confirmation of the results of cleft ion fountain analyses [*Lockwood et al*, 1985a, b; *Horwitz and Lockwood*, 1985; *Horwitz*, 1987]. The average O^+ density, bulk velocity, parallel temperature, perpendicular temperature, downward number flux, and upward number flux for total of 20 perigee passes (lower SZA regions only) are 7.7 (11.6) cm^{-3} , -0.9 (-1.1) km s^{-1} , 0.34 (0.29) eV , 0.61 (0.46) eV , 9.5×10^5 (1.2×10^6) $\text{cm}^{-2} \text{ s}^{-1}$, and 7.4×10^5 (7.9×10^5) $\text{cm}^{-2} \text{ s}^{-1}$, respectively.

We are also interested in the O^+/H^+ ratios for the various bulk parameters. Plots of O^+ versus H^+ in density, parallel velocity, and absolute number flux are shown in the left panels of Figure 10 and the O^+/H^+

density and parallel velocity ratio and absolute H^+/O^+ number flux ratio histograms are displayed in the right panels of Figure 10, where the solid lines represent the average ratios. In Figure 10, both H^+ and O^+ data are from low SZA regions only. The O^+/H^+ average density ratio is about 3.5, so O^+ is the dominant ion species at 5000 km altitude. The average H^+/O^+ absolute flux ratio is about 4.2, since H^+ ions have much higher velocities than O^+ ions. The O^+ velocities are primarily negative (downward) in our survey.

Plots of the perpendicular versus parallel temperatures for H^+ and O^+ are shown in the left top and bottom panels of Figure 11 and the parallel/perpendicular temperature ratio histograms for H^+ and O^+ are shown in the right top and bottom panels in Figure 11, where the solid lines represent the average ratios. The average parallel/perpendicular temperature ratios are 0.46 for H^+ ions and 0.58 for O^+ ions. The perpendicular temperatures tend to be about twice the parallel temperatures for both H^+ and O^+ ions ($T_{\perp i} \sim 2T_{\parallel i}$), which may suggest perpendicular ion heating at or below 5000 km altitude.

Plots of the O^+ versus H^+ temperatures are shown in the left panels and the ratio histograms are shown in the right panels in Figure 12, with parallel temperatures on the top panels and perpendicular temperatures on the bottom panels. The solid lines represent the average temperature ratios. The O^+ parallel temperature is on average 2.5 times higher than the H^+ parallel temperature and the O^+ perpendicular temperature is about twice that of H^+ , consistent with O^+ ions having generally higher energies than H^+ ions. This may be due in part to cleft ion fountain heating of O^+ .

H^+ (top) and O^+ (bottom) parallel Mach number histograms are shown in Figure 13, where the solid lines represent the average values. The H^+ Mach numbers range from 2.2 to 5 with the average at 3.7, which indicates that H^+ supersonic outflow exhibited at 5000 km altitude. The average O^+ Mach number is about -0.7 , indicating again O^+ subsonic downflow in general within the polar cap.

3.3 Relationship with Day-Night Distance in Solar Magnetic Coordinate System

The cleft ion fountain paradigm for O^+ would predict that the ion densities, parallel velocities, and parallel temperatures decrease from dayside to nightside [e.g., *Horwitz and Lockwood, 1985; Horwitz et al., 1985*]. An examination of the TIDE polar wind data versus the Sun-Earth axis in the Solar Magnetic

coordinate system (X_{SM}) was performed to investigate this suggestion. In the Solar Magnetic coordinate system, the z axis is chosen parallel to the north magnetic pole, the y axis is perpendicular to the Earth-Sun line toward dusk, and the x axis is in the other plane, positive towards the Sun. Plotting the data versus X_{SM} is equivalent to mapping the data to the noon-midnight plane of the polar magnetosphere. The H^+ ion densities, O^+ ion densities, O^+ parallel velocities, O^+ downward number fluxes, and O^+ parallel temperatures versus X_{SM} are shown in Figures 14 (a) – 14 (e). The straight lines in the H^+ and O^+ density plots are the linear least-square fits, using the logarithmically averaged densities at $0.11 R_E$ intervals in X_{SM} . Figure 14 (b) shows a very strong linear decline of O^+ densities with X_{SM} , with a high correlation coefficient, $r = 0.98$. The H^+ density correlation coefficient is 0.93 in (a), but again there is an uncertainty when the densities were less than 0.1 cm^{-3} . The O^+ densities and number fluxes increase from the nightside to the dayside, which would indicate a cleft ion fountain origin [Lockwood *et al.*, 1985; Horwitz and Lockwood, 1985], but the trends for the parallel velocities and parallel temperatures with X_{SM} are not conclusive.

4. Survey of $8 R_E$ Altitude Polar Wind with PSI Operation

When the POLAR satellite was near apogee in the northern hemisphere during 1996, the spacecraft typically attained large positive electric potentials of 40 V or more owing to the very low plasma densities in the high altitude polar cap as well as the photoelectron emission from the spacecraft. The Plasma Source Instrument (PSI) [Moore *et al.*, 1995] is a xenon plasma source, whose associated electrons balance the photoelectron escape-current and whose low electron temperature regulates the spacecraft potential to low values. The POLAR floating potential is monitored by Electric Field Instrument (EFI) [Harvey *et al.*, 1995] on POLAR, using three pairs of multi-element probes. Measurement of the resultant potential by EFI shows that the potential is stabilized at about $+1.8 - 2.2 \text{ V}$, when PSI was turned on, allowing TIDE measurements of low-energy ions in regions of very low plasma density [c.f., Moore *et al.*, 1997; Comfort *et al.*, 1997]. In order to observe this high altitude polar wind outflow, PSI operation is

necessary. Unfortunately, our polar wind survey at high altitude included only limited polar wind data at apogee from TIDE with PSI operating during the early portion of the POLAR mission. In this paper we focus on three long POLAR apogee passes in April and May, 1996. In summer, 1996, TIDE lost its mass analysis capability. Since then a considerable volume of polar wind data has been obtained with PSI running, but mass separation is not routinely possible and new analysis techniques will have to be developed for that data, which will be the subject of future studies.

Typical O^+ and H^+ ion distributions from 17:43:44 to 17:44:43 UT (one minute average) on April 19, 1996, are shown in Figures 15 (a) and (b). Since the apogee of the POLAR orbit was in the northern hemisphere, the negative x is in the direction along the magnetic field line away from Earth. In the left panel of Figure 15 (a), the phase space density distribution is sliced in the y - z plane perpendicular to the local magnetic field for an O^+ velocity of $V_x = -28.5 \text{ km s}^{-1}$. The right panel shows a slice in the parallel x - y plane with $V_z = -4.1 \text{ km s}^{-1}$. Likewise, a perpendicular plane of H^+ distribution with $V_x = -47.7 \text{ km s}^{-1}$ is seen in the left panel of Figure 15 (b), while the right panel shows a parallel plane with $V_z = -4.8 \text{ km s}^{-1}$. Both ion species were observed to be flowing out of the northern polar cap with high parallel velocities along the magnetic field lines. The spacecraft potential in this case was 1.94 V when PSI was operating. The O^+ and H^+ ion energies at apogee tend to be sufficient such that ion distributions were not significantly shielded by this residual 1.94 V spacecraft potential. The Poisson statistics error estimations associated with the individual measurements as discussed at the end of section 2 for this typical POLAR apogee case in Figure 15 are about 2.65% for H^+ (1426 counts per sample) and 8% for O^+ (156 counts per sample). However, other sources of errors may be larger.

In this section, we present polar wind characteristics and general trends in bulk parameters at POLAR apogee. We then discuss the relationship of parameters with day-night distance in the solar magnetic (SM) coordinate system at $8 R_E$ altitude. Each sample data here is averaged over one minute.

4.1 General Bulk Parameter Trends and Averages for the 8 R_E Polar Wind

The newly discovered polar wind from POLAR TIDE/PSI at 8 R_E altitude has several distinguishing characteristics, are shown in Figures 16 – 23, including densities, parallel velocities, number fluxes, and parallel and perpendicular temperatures for three ion species, H^+ , O^+ , and He^+ . We should note that the parameter estimates for He^+ in this paper are somewhat uncertain, since the He^+ data from TIDE were generally very close to the instrument noise level.

Occurrence frequency histograms for the H^+ polar wind parameters at 8 R_E altitude are shown in Figure 16, including density (top-left), parallel velocity (middle-left), parallel number flux (bottom-left), and parallel and perpendicular temperatures (two panels on the right), where the solid lines represent the average values. The H^+ densities range from 0.01 to 2 cm^{-3} with an average value of about 0.3 cm^{-3} , while the H^+ parallel velocities range from 20 to 110 $km\ s^{-1}$ with the average 45 $km\ s^{-1}$. All H^+ ions flow away from the Earth along magnetic field lines with a broad bulk flow velocity range. The H^+ outflow is a long-duration outflow which lasted for several hours at high altitudes over the polar cap. The H^+ parallel number flux was of order $10^5 - 10^7\ cm^{-2}\ s^{-1}$ with an average $1.2 \times 10^6\ cm^{-2}\ s^{-1}$. The average parallel and perpendicular temperatures for H^+ at high altitudes are about 1.7 and 1.1 eV ranging from 0.1 to 10 eV.

The corresponding occurrence frequency histograms for the O^+ polar wind parameters are shown in Figure 17, where the solid lines represent the average values again. The O^+ density was in the range $1 \times 10^{-3} - 0.3\ cm^{-3}$ with an average of 0.05 cm^{-3} , and the O^+ parallel velocity ranged between 8 and 32 $km\ s^{-1}$ with an average of about 17 $km\ s^{-1}$. At these high altitudes, all O^+ ions flow away from the Earth along the field lines. The O^+ parallel upward number flux ranged between 10^3 and $10^6\ cm^{-2}\ s^{-1}$ with an average of $8.3 \times 10^4\ cm^{-2}\ s^{-1}$. The average O^+ parallel and perpendicular temperatures are about 7.5 and 3.4 eV, both temperatures ranging from 0.2 to 30 eV.

The He^+ counts near apogee are often low and close to the instrument noise level, and thus at times provide unreliable bulk parameter estimates from the analysis procedure, in particular very low He^+ parallel and perpendicular temperatures (from 10^{-1} to 10^{-3} eV) for a number of He^+ samples. TIDE counts

respond to ion energy flux, and we found that when we examined the parallel and perpendicular temperatures versus He^+ energy density ($N \times T$), that the evidently-spurious temperatures occurred only for He^+ energy densities below $10^{-3} \text{ eV cm}^{-3}$ (using either parallel or perpendicular temperatures). Therefore, for the He^+ results in this paper, in Figures 18 – 21, we have only included He^+ bulk parameters for samples in which the parallel and perpendicular He^+ energy densities exceeded $10^{-3} \text{ eV cm}^{-3}$.

The He^+ density (left-top), parallel velocity (left-center), number flux (left-bottom), and parallel and perpendicular temperature (right two panels) histograms are shown in Figure 18. The He^+ density was in the range $10^{-3} - 0.1 \text{ cm}^{-3}$ with an average of 0.012 cm^{-3} , and the parallel velocity ranged between 8 and 63 km s^{-1} with an average upward velocity of about 25.4 km s^{-1} . The He^+ parallel number flux was in the range $10^3 - 10^5 \text{ cm}^{-2} \text{ s}^{-1}$ with an average of $2.5 \times 10^4 \text{ cm}^{-2} \text{ s}^{-1}$. The average parallel and perpendicular temperatures for He^+ were about 3.0 and 1.5 eV, respectively. The He^+ peak counts per sample (one-minute sample) was less than 25 counts, so the Poisson statistics uncertainty percentages are estimated to be larger than 20%.

In addition to the high altitude polar wind characteristics, we are also interested in the ratios of bulk parameters for these three ion species. The occurrence frequency histograms of density ratios for H^+ , O^+ , and He^+ are presented in log scale on the right in Figure 19, including O^+/H^+ (top-right), He^+/O^+ (middle-right), and He^+/H^+ (bottom-right) density ratios, where the solid lines represent the average density ratios. Plots of O^+ versus H^+ densities, He^+ versus O^+ densities, and He^+ versus H^+ densities are shown in the top, middle, and bottom panels on the left in Figure 19. The average O^+/H^+ density ratio was 0.16, while the average He^+/O^+ and He^+/H^+ ratios were 0.18 and 0.03. Figure 19 indicates that the H^+ ions were the highly dominant ion species at high altitudes. The average density ratios for these three ion species were $N_{\text{He}^+} : N_{\text{O}^+} : N_{\text{H}^+} \sim 1 : 6 : 38$, as summarized from Figure 19.

The occurrence frequency histograms of the velocity ratios for H^+ , O^+ , and He^+ are presented on the right in Figure 20, including O^+/H^+ (top-right), O^+/He^+ (middle-right), and He^+/H^+ (bottom-right) velocity ratios in linear scale, where the solid lines represent the average velocity ratios again. Plots of O^+ versus

H^+ velocities, O^+ versus He^+ velocities, and He^+ versus H^+ velocities are shown in the top, middle, and bottom panels on the left in Figure 20. The dashed lines in Figure 20 represent the equal energy gain ratios, $V_{O^+} : V_{He^+} : V_{H^+} = 1 : 2 : 4$, which would suggest equal energy gains for all three ions, such as via a photoelectron-driven electrostatic potential layer [Su *et al.*, 1998]. The average O^+/H^+ , O^+/He^+ , and He^+/H^+ velocity ratios were 0.40, 0.74, and 0.59. The average parallel velocity ratios for all three ion species were $V_{O^+} : V_{He^+} : V_{H^+} \sim 2 : 3 : 5$, as summarized from Figure 20. For velocity ratios near 1, the velocity filter (e.g., from the cleft ion fountain [Horwitz and Lockwood, 1985]) and/or centrifugal acceleration effects [Horwitz *et al.*, 1994] may be dominant. The observed ratios span all of these possibilities, so all of these effects — gravitational force, velocity filter, centrifugal acceleration, and electrostatic acceleration — may be involved in the transport of polar wind. The “typical” velocity ratios, $V_{O^+} : V_{He^+} : V_{H^+} \sim 2 : 3 : 5$, are somewhat more suggestive of the importance of comparable energy gains for the ion species.

The corresponding histograms for H^+ , O^+ , and He^+ number flux ratios are presented in log scale on the right in Figure 21, including O^+/H^+ (top-right), O^+/He^+ (middle-right), and He^+/H^+ (bottom-right) flux ratios, where the solid lines represent the average flux ratios. Plots of O^+ versus H^+ fluxes, O^+ versus He^+ fluxes, and He^+ versus H^+ fluxes are shown in the top, middle, and bottom panels on the left in Figure 21. The average O^+/H^+ , He^+/O^+ , and He^+/H^+ flux ratios were 0.06, 0.26, and 0.016. The average parallel number flux ratios were $F_{He^+} : F_{O^+} : F_{H^+} \sim 1 : 4 : 66$, as summarized from Figure 21. The H^+ outflow was the dominant ion outflow at POLAR apogee, while O^+ being second with the very low abundance of He^+ . The average number flux ratios for three ion species are not the classical polar wind abundance relationship.

Plots of the perpendicular versus parallel temperature for H^+ (top) and O^+ (bottom) are shown in the left panels, and the parallel/perpendicular temperature ratio histograms are shown in log scale on the right in Figure 22, where the solid lines represent the average temperature ratios. At POLAR apogee, the average parallel/perpendicular temperature ratios T_{\parallel}/T_{\perp} were about 1.4 for H^+ and 1.9 for O^+ . The parallel

temperatures were higher than the perpendicular temperatures for both H^+ and O^+ ions, $T_{\parallel i} > T_{\perp i}$, which is opposite from the behavior of the ion temperatures at 5000 km altitude. This is presumably because of the effects of conversion of perpendicular to parallel energy associated with (partial) conservation of the first adiabatic invariant along the diverging magnetic field lines.

In Figure 23, plots of the O^+ versus H^+ temperatures are shown in the left two panels and the O^+/H^+ temperature ratio histograms are shown in the right two panels, where the solid lines represent the average O^+/H^+ temperature ratios in both parallel (top) and perpendicular (bottom) directions. The O^+ parallel temperature is about 4.6 times the H^+ parallel temperature on average, while the perpendicular O^+/H^+ temperature ratio was about 3.4. O^+ ions have higher temperature than H^+ ions, $T_{O^+} > T_{H^+}$, in general. However, one factor which could work to lower the O^+ temperatures would be velocity-filtering from the narrow cleft ion fountain source [Horwitz *et al.*, 1985].

Figure 24 shows H^+ (top) and O^+ (bottom) parallel Mach number histograms at POLAR apogee, where the solid lines represent the average Mach numbers. The average H^+ Mach number was 4.6 ranging from about 2 to 7, and the average O^+ Mach number was 3.5 ranging from about 1 to 8. Both H^+ and O^+ flows were supersonic outflows at these high altitudes.

4.2 Relationship with Day-Night Distance in Solar Magnetic Coordinates at 8 R_E Altitude

The average bulk flow velocity ratios, $V_{O^+} : V_{He^+} : V_{H^+} \sim 2 : 3 : 5$, summarized from the previous subsection may suggest the importance of comparable energy gains for the ion species. However, the individually observed velocity ratios span a wide range, and may be consistent with varying contributions of such effects as gravitational force, velocity filter, centrifugal acceleration, and electrostatic acceleration, in the transport of polar wind. In order to reveal further aspects of the high-altitude bulk parameters, Figures 25 (a) and (b) show the O^+ and H^+ ion densities (top), parallel bulk velocities (middle), and parallel temperatures (bottom) versus X_{SM} . The ion densities decrease from the nightside to the dayside for three ion species, O^+ , H^+ , and He^+ (He^+ parameters versus X_{SM} is not shown here). Both O^+ and H^+ ion parallel velocities were higher on the dayside and ion densities declined from nightside to dayside, which

may suggest a cleft ion fountain origin. However, the parallel temperatures did not show the increasing trend from nightside to dayside which might be expected for a cleft ion fountain origin for these ions [c.f. *Horwitz and Lockwood, 1985*].

5. Summary and Discussion

Apparent from this study are several significant characteristics of polar wind at 5000 km and $8 R_E$ altitudes during April – May, 1996:

- (1) The polar wind density is dominantly O^+ at 5000 km altitude, but is strongly H^+ dominated at $8 R_E$ altitude. The He^+ ions play a very minor species in the polar wind.
- (2) The H^+ polar wind at 5000 km altitude is supersonic with an average velocity of 15 km s^{-1} , while O^+ is subsonic with an average velocity of -1 km s^{-1} , which is comparable with Akebono observations by *Abe et al. [1993a]* (see their Figure 3). At $8 R_E$ altitude, both H^+ and O^+ ion parallel flows are highly supersonic. The H^+ ion outflow spans a broad bulk flow velocity range from 20 to 110 km s^{-1} with an average velocity of about 45 km s^{-1} , while O^+ ion velocities ranged from 8 to 32 km s^{-1} with an average velocity of about 27 km s^{-1} , which is faster than that predicted by some polar wind models [e.g., *Gombosi and Killeen, 1987; Wilson et al., 1990; Demars and Schunk, 1991; Ho et al., 1993*].
- (3) The perpendicular temperature is higher than the parallel temperature at 5000 km altitude for both H^+ and O^+ , which may suggest perpendicular ion heating though wave-particle interactions [e.g., *Ganguli and Palmadesso, 1987; Demars and Schunk, 1987, 1989; Chen and Ashour-Abdalla, 1990; Brown et al., 1991; Barakat and Barghouthi, 1994; Demars et al., 1998*]. At $8 R_E$ altitude, the parallel temperature is higher than the perpendicular temperature, which is likely due to the adiabatic conversion of perpendicular to parallel energy in the outward flow along the diverging magnetic field lines. The high-altitude ion temperature anisotropy, $T_{\parallel i} > T_{\perp i}$, is presumably due to the (partial) conservation of the magnetic moment, and is consistent with various polar wind calculations [e.g.,

Schunk and Watkins, 1982; Ganguli et al., 1987; Demars and Schunk, 1987, 1989, 1994] while at low altitudes, the ion temperature anisotropies are reversed to $T_{\perp i} > T_{\parallel i}$ as noted above.

- (4) The O^+ temperatures are higher than the H^+ temperatures at both low and high altitudes. The observed ion temperatures are higher than found in any of the modeling results, unless hot ions are put in at the bottom of the simulation.

Horwitz and Lockwood [1985] showed that energy separation should occur in the ions transported from the ionospheric cleft energization region as they are convected across the polar cap. This could lead to a region of divergent flow marking the boundary between escaping and gravitationally bound ions. Thus, it is to be expected that O^+ of ionospheric origin should be observable moving both upward and downward along polar cap field lines. Our O^+ polar wind survey has indicated downflowing O^+ ions at 5000 km altitude and upflowing O^+ ions at $8 R_E$ altitude, which is consistent with the cleft ion fountain paradigm [*Horwitz and Lockwood, 1985*]. Significant O^+ downflows in the polar cap were observed from DE 1/RIMS by *Chandler [1995]* and were also obtained using a global ionosphere-polar wind model [*Schunk and Sojka, 1997*]. Our H^+ polar wind measurements showing supersonic characteristics (the Mach number ranged from 2.2 to 5) are consistent with DE 1 observations [*Nagai et al., 1984*], which included Mach numbers ranging from 2.6 to 5.1, in general accord with “classical” polar wind model results [e.g., *Banks and Holzer, 1969; Lemaire and Scherer, 1970*].

Abe et al. [1993a] found that the ion velocity and temperature distributions from Akebono exhibited a day-to-night asymmetry (see their Figures 4 and 5). From our TIDE polar wind survey, the day-night asymmetry was seen only in densities, which decreased from dayside to nightside, but not the velocity and temperature at low altitude (see our Figure 14). Our average O^+ velocity at 5000 km altitude, -1 km s^{-1} , is consistent with *Abe et al. [1993a]* results (see their Figure 3), however, our average H^+ velocity, 15 km s^{-1} , is somewhat higher than their average of about 8 km s^{-1} . At Akebono apogee (10,000 km), the average velocity ratios for O^+ , He^+ , and H^+ were about $2 : 3.5 : 6$, which is comparable to TIDE polar wind observations, $V_{O^+} : V_{He^+} : V_{H^+} \sim 2 : 3 : 5$, at POLAR apogee. At an altitude of $8 R_E$, the ion densities

decline from nightside to dayside while the ion velocities are larger on the dayside. No significant trend is seen for temperatures (see our Figure 25).

Dramatic decreases of the 5000 km altitude H^+ and O^+ densities and fluxes are seen from 90° to 110° solar zenith angle for the ionospheric base. This is consistent with solar illumination ionization control. On the other hand, the downward O^+ flow and the O^+ densities decrease from dayside to nightside which suggest the cleft ion fountain origin for the polar cap O^+ [Lockwood *et al*, 1985; Horwitz *et al* and Lockwood, 1985]. The O^+ densities are indeed highly correlated ($r = 0.98$) with X_{SM} . From our survey of the polar wind at low altitude, one conclusion would be that the solar zenith angle controls the H^+ polar wind in the polar cap, but the cleft ion fountain controls the polar cap O^+ . The strongest evidence for cleft ion fountain controlled is actually the downward O^+ flow at 5000 km in polar cap. However, it may even be possible that the spread of cleft ion fountain O^+ influences the day-night variations of the H^+ polar wind as much or more than the direct solar illumination of the F region ionosphere, since the correlation coefficients for H^+ densities versus solar zenith angle and X_{SM} are similar, and the H^+ and O^+ densities are correlated with a correlation coefficient $r = 0.8$ (shown in Figure 26). Enhanced upward flows of O^+ and enhanced O^+ densities in the cleft region are observed in the F region and topside ionosphere [e.g., Loranc *et al.*, 1991]. These would lead to enhanced O^+ extending from the cleft toward the center of the polar cap at altitudes down into the F region, which is where accidentally-resonant charge exchange reaction, $O^+ + H \rightarrow H^+ + O$, takes place to produce ionospheric H^+ . Thus, the elevated densities of O^+ in the topside ionosphere (≤ 1000 km) toward the dayside (which we think are associated with the cleft ion fountain processes) could indirectly also control the dayside increase of H^+ densities via this charge-exchange processes within the low altitude transition region. It will be interesting to further distinguish the cleft ion fountain and solar illumination controlling influences on the polar wind in further data analyses, as well as modeling investigations.

In addition to the polar wind characteristics and the relationship with SZA and X_{sm} , we have also investigated the possible relationship of the TIDE polar wind parameters with magnetic activity (e.g., K_p).

No clear correlation which K_p has found from our survey (limited passes during April and May, 1996). For the 20 perigee passes in April, 1996, The K_p index varied in between 1– and 5. Coincidentally, the higher K_p (3–5) appeared at low SZA ($< 100^\circ$) passes and the lower K_p (1–3) appeared at the high SZA passes. The K_p index was 3+ to 5 at POLAR apogee on April 19, 1996, and was 1– to 1 at apogee on May 28, 1996. Moreover, there is no clear relationship with the IMF B_z component, either. We conclude from that the IMF and K_p produce no strong effect on the polar wind proper, which we have base our polar wind measurements on. Since we have used the more energetic particle signatures to restrict our measurements already to the polar cap field lines regardless of the high-latitude auroral topology, it is not especially surprising that the physics of the polar wind might be insensitive to the IMF and K_p levels. On the other hand, we believe that O^+ ions at POLAR perigee are from the cleft region which could be influenced by the IMF and K_p . However, we find no strong correlation with IMF and K_p on O^+ flows at POLAR perigee.

H^+ and O^+ densities and O^+ number fluxes decrease from the dayside to the nightside with O^+ downward flow at 5000 km altitude. At $8 R_E$ altitude, H^+ and O^+ densities declined from the nightside to the dayside, while velocities increased from nightside to dayside. These may suggest cleft ion fountain origin. However, the “typical” parallel velocity ratios from TIDE high altitude observations, $V_{O^+} : V_{He^+} : V_{H^+} \sim 2 : 3 : 5$, may suggest the importance of comparable energy gains, such as via a photoelectron-driven electric potential layer. Several mechanisms for energizing and driving the polar plasma outflows have been studied, such as photoelectron effects [e.g., *Lemaire*, 1972; *Winningham and Gurgiolo*, 1982; *Horwitz et al*, 1992; *Abe et al.*, 1993a, b; *Tam et al.*, 1995; *Yau et al.*, 1995; *Wilson et al.*, 1997; *Su et al.*, 1998], hot magnetospheric electrons, such as the polar rain, showers, and squall [e.g., *Barakat and Schunk*, 1984; *Ho et al.*, 1992; *Su et al.*, 1998], and centrifugal acceleration associated with convection [e.g., *Cladis*, 1986; *Swift*, 1990; *Horwitz et al.*, 1994; *Demars et al.*, 1996].

Horwitz et al. [1994], using a steady state semikinetic model, demonstrated that centrifugal acceleration can be an effect of zeroth-order importance in describing the convecting polar wind if convection is strong. The O^+ velocity at $8 R_E$ geocentric distance increased from 1 km s^{-1} to 8, 30, and 60

km s^{-1} for ionospheric convection electric fields increasing from 0 to 10, 50, and 100 mV/m (see their Figure 6), while the H^+ velocity increased to 36, 48, and 72 km s^{-1} (see their Figure 5). Our observed parallel velocities of the polar wind at $8 R_E$ altitude are generally comparable to their results when the convection (centrifugal force) was turned on. They further suggested that the field-aligned and convection flow energies would be equal if the streams were accelerated only by such a centrifugal force. This problem requires additional investigation [Elliott *et al.*, 1997].

A comparison of our range of observed parameters from POLAR/TIDE with the photoelectron-driven polar wind model of Su *et al.* [1998] (an electric double layer-associated discontinuity near $3.5 R_E$) and the “base-line” polar wind results by a coupled fluid-semikinetik transport simulation for solar minimum conditions is shown in Figure 27. The horizontal solid and dashed lines in the middle and right panels are the observed ranged of parallel velocities and densities from TIDE observations for H^+ and O^+ ions, respectively, at 5000 km and $8 R_E$ altitudes. The polar wind densities and parallel velocities from TIDE observations are comparable to the Su *et al.* [1998] simulation results in general. The H^+/O^+ parallel velocity ranges observed by TIDE extend from the base line polar wind value up to and beyond that of the photoelectron-driven polar wind velocity at $8 R_E$ altitude. This may indicate variations of the photoelectron fluxes from the ionosphere or downward magnetospheric electrons (such as polar rain, showers, squalls). Such variations could cause the suggested electrostatic double layer to vary in amplitude and altitude. Persoon *et al.* [1983] indicated the electron density variations in the polar cap from DE 1 plasma wave observations. Barakat and Schunk [1983, 1984] and Ho *et al.* [1992], using semikinetik simulations, also indicated that the polar wind outflows vary with electron temperature and density. More recently, Barakat *et al.* [1997] presented O^+ density and velocity variations at high altitudes using a time-dependent semikinetik polar wind simulation, including hot electron effects, with the ionospheric conditions input from a low-altitude ionosphere-atmosphere model [Schunk and Sojka, 1989]. Therefore, it would be useful to analyze low-energy electron data from the HYDRA instrument on POLAR and examine the possible effects of the polar rain and photoelectrons. Combining the TIDE polar wind observations with HYDRA

electron data may assist in understanding the large variation in the ion parallel flow velocities observed at very high altitudes.

The survey results to date are consistent with the concept derived from Dynamics Explorer (DE) 1 of a "fountain in a wind" of O^+ and more energetic light ions emanating from the dayside auroral oval, while also exhibiting characteristics that are familiar from theoretical descriptions of a thermal polar wind, independent of any auroral energy inputs. The survey clearly indicates a direction for future polar wind modeling studies, which should account for the closed circulation of polar plasma tubes with auroral energy inputs upon passage through the dayside and nightside auroral zones. A general simulation could be performed in which a particular flux tube is followed through a full convection cycle as an open flux tube convecting over the polar cap. The flux tube could be then allowed to close into an extended closed flux tube which convects into the auroral zone-plasma sheet through the dusk or dawn magnetosphere. It would eventually convect back through the cleft/cusp region before again becoming an open flux tube in the polar region [e.g., *Schunk and Sojka*, 1989, 1997; *Demars et al.*, 1996, 1998].

Acknowledgments. This work was supported by the NASA Global Geospace Science Program at Goddard Space Flight Center under UPN 370-17-43, by the NASA Office of Space Flight at Marshall Space Flight Center, and by NASA grant NCC8-65 and NSF grant ATM-9301024 to the University of Alabama in Huntsville. The authors are indebted to the technical staffs of their institutions and those of the Los Alamos National Laboratories, the Hughes Research Laboratories, the Centre d'Etudes Terrestre et Planetaire, and the Computer Sciences Corporation for the development of the TIDE and PSI hardware and software. The authors acknowledge valuable discussions with A. R. Barakat and A. W. Yau.

References

- Abe, T., B. A. Whalen, A. W. Yau, R. E. Horita, S. Watanabe, and E. Sagawa, EXOS D (Akebono) suprathermal mass spectrometer observations of the polar wind, *J. Geophys. Res.*, **98**, 11191, 1993a.
- Abe, T., B. A. Whalen, A. W. Yau, S. Watanabe, E. Sagawa, and K. I. Oyama, Altitude profile of the polar wind velocity and its relationship to ionospheric conditions, *Geophys. Res. Lett.*, **20**, 2825, 1993b.
- Acuña, M. H., K. W. Ogilvie, D. N. Baker, S. A. Curtis, D. H. Fairfield, and W. H. Mish, The global geospace science program and its investigations, *Space. Sci. Rev.*, **71**(1-4), 21, 1995.
- Banks, P. M., and T. E. Holzer, Features of plasma transport in the upper atmosphere, *J. Geophys. Res.*, **74**, 6304, 1969.
- Barakat, A. R., and I. A. Barghouthi, The effect of wave-particle interaction on the polar wind O^+ , *Geophys. Res. Lett.*, **21**, 2279, 1994.
- Barakat, A. R., and R. W. Schunk, O^+ ions in the polar wind, *J. Geophys. Res.*, **88**, 7887, 1983.
- Barakat, A. R., and R. W. Schunk, Effect of hot electrons on the polar wind, *J. Geophys. Res.*, **89**, 9771, 1984.
- Barakat, A. R., H. G. Demars, and R. W. Schunk, Temporal behavior of the polar wind in the presence of hot electrons(abstract), *Eos Trans. AGU*, **78**(46), F502, 1997.
- Brinton, H. C., J. M. Grebowsky, and H. G. Mayr, Altitude variation of ion composition in the midlatitude trough region: evidence for upward plasma flow, *J. Geophys. Res.* **76**, 3738, 1971.
- Brown, D. G., G. R. Wilson, J. L. Horwitz, and D. L. Gallagher, "Self-consistent" production of ion conics on return current region auroral field lines: A time-dependent, semikinetic model, *Geophys. Res. Lett.*, **18**, 1841, 1991.
- Chandler, M. O., Observations of downward moving O^+ in the polar topside ionosphere, *J. Geophys. Res.*, **96**, 5795, 1995.

- Chandler, M. O., J. H. Waite Jr., and T. E. Moore, Observations of polar ion outflows, *J. Geophys. Res.*, **96**, 1421, 1991.
- Chen, M. W., and M. Ashour-Abdallah, Heating of the polar wind due to ion beam instabilities, *J. Geophys. Res.*, **95**, 18949, 1990.
- Cladis, J. B., Parallel acceleration and transport of ions from polar ionosphere to plasma sheet, *Geophys. Res. Lett.*, **13**, 893, 1986.
- Comfort, R. H., T. E. Moore, P. D. Craven, C. J. Pollock, F. S. Mozer, and W. T. Williamson, Spacecraft potential control by PSI on the POLAR satellite, *J. Spacecraft and Rockets*, in review, 1998.
- Demars, H. G., and R. W. Schunk, Temperature anisotropies in the terrestrial ionosphere and plasmasphere, *Rev. Geophys.*, **25**, 1659, 1987.
- Demars, H. G., and R. W. Schunk, solutions to bi-Maxwellian transport equations for the polar wind, *Planet. Space Sci.*, **37**, 85, 1989.
- Demars, H. G., and R. W. Schunk, Comparison of semikinetic and generalized transport models of the polar wind, *Geophys. Res. Lett.*, **18**, 713, 1991.
- Demars, H. G., and R. W. Schunk, A multi-ion generalized transport model of the polar wind, *J. Geophys. Res.*, **99**, 2215, 1994.
- Demars, H. G., A. R. Barakat, and R. W. Schunk, Effect of centrifugal acceleration on the polar wind, *J. Geophys. Res.*, **101**, 24,565, 1996.
- Demars, H. G., A. R. Barakat, and R. W. Schunk, Trapped particles in the polar wind, *J. Geophys. Res.*, **103**, 419, 1998.
- Dessler, A. J., and P. A. Cloutier, Discussion of letter by Peter M. Banks and Thomas E. Holzer, "The polar wind", *J. Geophys. Res.*, **74**, 3730, 1969.
- Elliott, H. A., et al., Ion outflow and convection in the polar cap and cleft as measured by TIDE, EFI, MFE, and TIMAS on POLAR(abstract), *Eos Trans. AGU*, **78**(46), F623, 1997.
- Ganguli, S. B., The polar wind, *Rev. Geophys.*, **34**, 311, 1996.

- Ganguli, S. B., and P. J. Palmadesso, Plasma transport in the auroral return current region, *J. Geophys. Res.*, 92, 8673, 1987.
- Ganguli, S. B., H. G. Mitchell, and P. J. Palmadesso, Behavior of ionized plasma in the high latitude topside ionosphere: The polar wind, *Planet. Space Sci.*, 35, 703, 1987.
- Gombosi, T. I., and T. L. Killeen, Effects of thermospheric motions on the polar wind: A time-dependent numerical study, *J. Geophys. Res.*, 92, 4725, 1987.
- Gombosi, T. I., and R. W. Schunk, A comparative study of plasma expansion events in the polar wind, *Planet. Space Sci.*, 36, 753, 1988.
- Gombosi, T. I., T. E. Cravens, and A. F. Nagy, A time-dependent theoretical model of the polar wind : Preliminary results, *Geophys. Res. Lett.*, 12, 167, 1985.
- Gurgiolo, C., and J. L. Burch, DE-1 observations of the polar wind — a heated and an unheated component, *Geophys. Res. Lett.*, 9, 945, 1982.
- Gurnett, D. A., et al., the Polar Plasma Wave Instrument, *Space Sci. Rev.*, 71(1-4), 597, 1995.
- Harvey, P. J., et al., The electric field instrument on the POLAR spacecraft, *Space Sci. Revs.*, 71(1-4), 583, 1995.
- Ho, C. W., J. L. Horwitz, G. R. Wilson, N. Singh, and T. E. Moore, Effects of magnetospheric electrons on polar plasma outflow: A semikinetic model, *J. Geophys. Res.*, 97, 8425, 1992.
- Ho, C. W., J. L. Horwitz, N. Singh, and G. R. Wilson, Plasma expansion of density perturbations in the polar wind: comparison of semikinetic and transport models, *J. Geophys. Res.*, 98, 13,581, 1993.
- Hoffman, J. H., Studies of the composition of the ionosphere with a magnetic deflection mass spectrometer, *Int. J. Mass Spectrum. Ion Phys.*, 4, 315, 1970.
- Hoffman, J. H., W. H. Dodson, C. R. Lippincott, and H. D. Hammack, Initial ion composition results from ISIS 2 satellite, *J. Geophys. Res.*, 79, 4246, 1974.
- Hoffman, J. H. and W. H. Dodson, Light ion concentrations and fluxes during magnetically quiet times, *J. Geophys. Res.*, 85, 626, 1980.

- Horwitz, J. L., The ionosphere as a source for magnetospheric ions, *Rev. Geophys. Spc. Phys.*, 20, 929, 1982.
- Horwitz, J. L., Features of ion trajectories in the polar magnetosphere, *Geophys. Res. Lett.*, 11, 1111, 1984.
- Horwitz, J. L., Core plasma in the magnetosphere, *Rev. Geophys. Spc. Phys.*, 25, 579, 1987.
- Horwitz, J. L., The ionosphere's wild ride in outer space, *Rev. Geophys.*, 33, 703, 1995.
- Horwitz, J. L., and M. Lockwood, The cleft ion fountain: a two-dimensional kinetic model, *J. Geophys. Res.*, 90, 9749, 1985.
- Horwitz, J. L., and T. E. Moore, Four contemporary issues concerning ionospheric plasma flow to the magnetosphere, *Space Sci. Rev.*, 80, 49, 1997.
- Horwitz, J. L., C. J. Pollock, T. E. Moore, W. K. Peterson, J. L. Burch, J. D. Winningham, J. D. Craven, L. A. Frank, and A. Persoon, The polar cap environment of outflowing O^+ , *J. Geophys. Res.*, 97, 8361, 1992.
- Horwitz, J. L., C. W. Ho, H. D. Scarbro, G. R. Wilson, and T. E. Moore, Centrifugal acceleration of the polar wind, *J. Geophys. Res.*, 99, 15,051, 1994.
- Lemaire, J., Effect of escaping photoelectrons in a polar exospheric model, *Space Res.*, 12, 1413, 1972.
- Lemaire, J., and M. Scherer, Model of the polar ion-exosphere, *Planet. Space Sci.*, 18, 103, 1970.
- Lockwood, M., J. H. Waite Jr., T. E. Moore, J. F. E. Johnson, and C. R. Chappell, A new source of suprathermal O^+ ions near the dayside polar cap boundary, *J. Geophys. Res.*, 90, 4099, 1985a.
- Lockwood, M., M. O. Chandler, J. L. Horwitz, J. H. Waite, Jr., T. E. Moore, and C. R. Chappell, The cleft ion fountain, *J. Geophys. Res.*, 90, 9736, 1985b.
- Loranc, M., W. B. Hanson, R. A. Heelis, and P.-P. St.-Maurice, A morphological study of vertical ionospheric flows in the high-latitude F region, *J. Geophys. Res.*, 96, 3627, 1991.
- Moore, T. E., et al., The thermal ion dynamics experiment and plasma source instrument, *Space Sci. Rev.*, 71(1-4), 409, 1995.

- Moore, T. E., M. O. Chandler, C. J. Pollock, D. L. Reasoner, R. L. Arnoldy, B. Austin, P. M. Kintner, and J. Bonnell, Plasma heating and flow in an auroral arc, *J. Geophys. Res.*, *101*, 5279, 1996.
- Moore, T. E., et al., High altitude observations of the polar wind, *Science*, *277*, 349, 1997.
- Nagai, T., J. H. Waite, Jr., J. L. Green, C. R. Chappell, R. C. Olsen, and R. H. Comfort, First measurements of supersonic polar wind in the polar magnetosphere, *Geophys. Res. Lett.*, *11*, 669, 1984.
- Olsen, R. C., C. R. Chappell, and J. L. Burch, Aperture plane potential control for thermal ion measurements, *J. Geophys. Res.*, *91*, 3117, 1986.
- Persoon, A. M., D. A. Gurnett, and S. D. Shawhan, Polar cap electron densities from DE 1 Plasma wave observations, *J. Geophys. Res.*, *88*, 10,123, 1983.
- Pollock, C. J., M. O. Chandler, T. E. Moore, J. H. Waite, Jr., C. R. Chappell, and D. A. Gurnett, A survey of upwelling ion event characteristics, *J. Geophys. Res.*, *95*, 18,969, 1990.
- Raitt, W. J., R. W. Schunk, and P. M. Banks, A comparison of the temperature and density structure in the high and low speed thermal proton flows, *Planet. Space Sci.*, *23*, 1103, 1975.
- Schunk, R. W., and J. J. Sojka, , A three-dimensional time-dependent model of the polar wind, *J. Geophys. Res.*, *94*, 8973, 1989.
- Schunk, R. W., and J. J. Sojka, Global ionosphere-polar wind system during changing magnetic activity, *J. Geophys. Res.*, *102*, 11,625, 1997.
- Schunk, R. W., and D. S. Watkins, Electron temperature anisotropy in the polar wind, *J. Geophys. Res.*, *86*, 91, 1981.
- Schunk, R. W., and D. S. Watkins, Proton temperature anisotropy in the polar wind, *J. Geophys. Res.*, *87*, 171, 1982.
- Shelley, E. C., W. K. Peterson, A. G. Ghielmetti, and J. Geiss, The polar ionosphere as a source of energetic magnetospheric plasma, *Geophys. Res. Lett.*, *9*, 941, 1982.

- Swift, D. W., Simulation of the ejection of plasma from the polar ionosphere, *J. Geophys. Res.*, 95, 12103, 1990.
- Su, Y.-J., J. L. Horwitz, G. R. Wilson, P. G. Richards, D. G. Brown, and C. W. Ho, Self-consistent simulation of the photo-electron-driven polar wind from 120 km to 9 R_E altitude, *J. Geophys. Res.*, 103, 2279, 1998.
- Tam, S. W. Y., F. Yasseen, T. Chang, and S. B. Ganguli, Self-consistent kinetic photoelectron effects on the polar wind, *Geophys. Res. Lett.*, 22, 2107, 1995.
- Waite, J. H. Jr., T. Nagai, J. F. E. Johnson, C. R. Chappell, J. L. Burch, T. L. Killeen, P. B. Hays, G. R. Carignan, W. K. Peterson, and E. G. Shelley, Escape of suprathermal O⁺ ions in the polar cap, *J. Geophys. Res.*, 90, 1619, 1985.
- Wilson, G. R., Semikinetic modeling of the outflow of ionospheric plasma through the topside collisional to collisionless transition region, *J. Geophys. Res.*, 97, 10,551, 1992.
- Wilson, G. R., C. W. Ho, J. L. Horwitz, N. Singh, and T. E. Moore, A new kinetic model for time-dependent polar plasma outflow: Initial results, *Geophys. Res. Lett.*, 17, 263, 1990.
- Wilson, G. R., G. Khazanov, and J. L. Horwitz, Achieving zero current on open flux tubes carrying large photoelectron fluxes, *Geophys. Res. Lett.*, 24, 1183, 1997.
- Winningham, J. D., and C. Gurgiolo, DE-2 photoelectron measurements consistent with a large scale parallel electric field over the polar cap, *Geophys. Res. Lett.*, 9, 977, 1982.
- Yau, A. W., B. A. Whalen, W. K. Peterson, and E. G. Shelley, Distribution of upflowing ionospheric ions in the high-altitude polar cap and auroral ionosphere, *J. Geophys. Res.*, 89, 5507, 1984.
- Yau, A. W., T. Abe, T. Chang, T. Mukai, K. I. Oyama, and B. A. Whalen, Akebono observations of electron temperature anisotropy in the polar wind, *J. Geophys. Res.*, 100, 17451, 1995.

Figure 1. H^+ (top panel) and O^+ (bottom panel) ion flux data are plotted after averaging over 42 seconds (7 spins) intervals, which are bounded by white tic marks at POLAR perigee from 03:20:00 to 03:50:00 UT on April 4, 1996. The energy flux is color coded (10^2 to 10^8 $eV s^{-1} cm^{-2} sr^{-1} eV^{-1}$ as indicated by the vertical brightness bar) versus polar angle (0° to 157.5°), spin azimuth angle (0° to 360° , along the vertical axis), and energy. The color wheel indicates the interpretation of colors as energy distributions (red for the low energy from 0 to 3 V, green for the energy from 3 to 30 V, and blue for the high energy from 30 to 100 V). Universal time (UT), spacecraft geocentric radius (R_e), L shell (Lshell), magnetic local time (mlt), magnetic latitude (mlat), and invariant latitude (inflat) are indicated along the horizontal axis. The spin angle closest to the magnetic field direction and its opposite are indicated by plus and minus signs, while the spacecraft velocity spin angle is indicated by “x” signs.

Figure 2. Typical phase space density velocity distribution for O^+ (a) and H^+ (b) at perigee from 03:34:57 to 03:35:56 UT on April 23, 1996, where the x axis is the local magnetic field direction, the y axis is the normal vector lying in the spacecraft orbit plane, and the z axis is orthogonal to the x and y axis. In Figure 2 (a), the phase spaced density distribution is sliced in the plane perpendicular to the local magnetic field for an O^+ velocity of $V_x = -1.1$ $km s^{-1}$. The right panel shows a slice in the parallel plane with $V_z = -0.8$ $km s^{-1}$. Likewise, a perpendicular plane of H^+ distribution with $V_x = 15.8$ $km s^{-1}$ is seen in the left panel of Figure 2 (b), while the right panel shows a parallel plane with $V_z = -4.5$ $km s^{-1}$. The phase space density is contoured as indicated by the saturated gray-scale bar on the right. The tic mark indicate the spacecraft frame of reference (fine black), the Earth frame of reference (white) and the computed plasma frame (bold black). The velocity and gray-scale bar ranges differ between the O^+ and H^+ panels. The distributions are shielded by the spacecraft potential estimated to be 1.73 V here, especially the H^+ distributions in (b). The approximate region for the velocity space integration is discussed in the text.

Figure 3. The flowchart of the bi-Maxwellian filling-in procedure.

Figure 4. The H^+ phase space density velocity distribution after the iterated “filling” technique, starting from the distribution displayed in Figure 2 (b). The phase space density is contoured as indicated by the

saturated gray-scale bar at center, which is the same gray-scale bar as in Figure 2 (b). Note: the moments are only calculated over the same region of velocity space as in Figure 2 (b), so that the outlying velocity space regions do not contribute to the moments.

Figure 5. H^+ and O^+ bulk parameters, including density, velocity along the local magnetic field line (V_x , circles), velocity of the normal vector lying in the spacecraft orbit plane (V_y , squares), velocity component orthogonal to x and y axis (V_z , triangles), and the temperatures parallel (circles) and perpendicular (squares) to the local magnetic field, are plotted at one minute intervals using the analysis technique described above, for one typical POLAR perigee pass from 05:13:35-05:26:05 UT on April 20, 1996. Universal time (UT), spacecraft geocentric radius (R_e), L shell (Lshell), magnetic local time (mlt), magnetic latitude (mlat), and invariant latitude (invlat) are indicated along the horizontal axis. The open symbols represent the parameters for O^+ ions, while the closed symbols represent the parameters for H^+ ions.

Figure 6. The photoelectron number flux at 800 km altitude (top panel) and O^+ density at 500 km altitude (bottom panel) versus solar zenith angle from the coupled fluid-semikinetik model [Su *et al.*, 1998].

Figure 7. The H^+ and O^+ bulk parameters, including H^+ (a) and O^+ densities (b) in log scale, H^+ (c) and O^+ bulk velocities (d), O^+/H^+ density ratios (e), H^+ (f) and O^+ number fluxes (g), versus the solar zenith angle. The solid triangles are the linearly averaged values, the open triangles are the logarithmically averaged densities at 5 degree intervals in SZA. The vertical bar is the standard deviation in log scale in panels (a) and (b), and in the linear scale in panels (c) and (d). The solid triangles are the average values including both downward (the bottom panel in g) and upward fluxes (the top panel in g) for O^+ in panel (g) at 5 degree intervals in SZA. The straight lines in (a) and (b) are the linear least-square fits in log scale from the average density values. The correlation coefficients (r) with SZA are 0.93 for the H^+ density and 0.95 for the O^+ density.

Figure 8. The occurrence frequency histograms for the H^+ bulk parameters, including density (top-left), parallel velocity (mid-left), parallel number flux (bottom-left), and parallel and perpendicular temperature (two panels on the right) at 5000 km altitude. The vertical solid lines represent the average values.

Figure 9. The occurrence frequency histograms for the O^+ bulk parameters, including density (top-left), parallel velocity (mid-left), parallel temperature (top-right), perpendicular temperature (mid-right), and downward and upward number fluxes (bottom-left and bottom-right) at 5000 km altitude. The lines with the solid circles are the occurrence frequencies based on 20 perigee passes with the average values shown as the vertical solid lines. The line with the open circles is the occurrence summed from the data at low solar zenith angle ($SZA < 110^\circ$) region only, with the average values shown as vertical dashed lines.

Figure 10. The occurrence frequency histograms for the O^+/H^+ density ratios (top-right), parallel velocity ratios (middle-right), and the absolute number flux ratios (bottom-right) are shown on the right panels. The density and number flux ratio histograms are in log scale. The O^+ versus H^+ bulk parameters, including densities (top-left), bulk velocities (middle-left), and absolute density fluxes (bottom-left) are shown on the left panels. The solid lines represent the average values.

Figure 11. The occurrence frequency histograms for the parallel/perpendicular temperature ratios for H^+ (top-right) and O^+ (bottom-right) in log scale are shown on the right panels. The plots on the left panels are the parallel temperature versus perpendicular temperature for H^+ (top-left) and O^+ (bottom-left). The solid lines represent the average values.

Figure 12. The occurrence frequency histograms for the O^+/H^+ parallel and perpendicular temperature ratios in log scale are shown on the right panels. The plots on the left panels are the O^+ versus H^+ temperature for both parallel and perpendicular components. The solid lines represent the average values.

Figure 13. The Mach numbers histograms for polar cap H^+ (top) and O^+ (bottom) at 5000 km altitude. The solid lines represent the average Mach numbers.

Figure 14. The bulk parameters, including H^+ densities (a), O^+ densities (b), O^+ velocities (c), O^+ downward fluxes (d), and O^+ parallel temperatures (e) versus X_{SM} . The open triangles with solid lines are

the values averaged over the interval of $0.11 R_E$ in X_{SM} . The straight lines in (a) and (b) are the linear least-square fits in the log scale from the average density points. The correlation coefficients are 0.93 for H^+ density and 0.98 for O^+ densities.

Figure 15. The typical phase space density velocity distribution for O^+ (a) and H^+ (b) at apogee from 17:43:44 to 17:44:43 UT on April 19, 1996. The coordinate system is defined similar to the discussion of Figure 2. In Figure 15 (a), the phase spaced density distribution is sliced in the plane perpendicular to the local magnetic field for an O^+ velocity of $V_x = -28.5 \text{ km s}^{-1}$. The right panel shows a slice in the parallel plane with $V_z = -4.1 \text{ km s}^{-1}$. Likewise, a perpendicular plane of H^+ distribution with $V_x = -47.4 \text{ km s}^{-1}$ is seen in the left panel of Figure 15 (b), while the right panel shows a parallel plane with $V_z = -4.8 \text{ km s}^{-1}$. Here, the negative V_x means the polar wind is flowing outward from the Earth along the magnetic field lines in the northern hemisphere. The velocity scales differ between the O^+ and H^+ panel. The spacecraft potential is 1.94 V in this case.

Figure 16. The histograms for H^+ bulk parameters, including densities (top-left), parallel velocities (mid-left), number fluxes (bottom-left), and parallel and perpendicular temperatures (two panels on the right) at $8 R_E$ altitude. The vertical solid lines represent the average values.

Figure 17. The histograms for O^+ bulk parameters, including densities (top-left), parallel velocities (mid-left), number fluxes (bottom-left), and parallel and perpendicular temperatures (two panels on the right) at POLAR apogee. The vertical solid lines represent the average values.

Figure 18. The histograms for He^+ bulk parameters, including densities (top-left), parallel velocities (mid-left), number fluxes (bottom-left), and parallel and perpendicular temperatures (two panels on the right) at $8 R_E$ altitude. The vertical solid lines represent the average values.

Figure 19. The left panels are the O^+ versus H^+ density on the top, He^+ versus O^+ density in the middle, and He^+ versus H^+ density at the bottom. The right panels are O^+/H^+ (top), He^+/O^+ (middle), He^+/H^+ (bottom) density ratio histograms in log scale. The solid lines represent the average density ratios.

Figure 20. The left panels are the O^+ versus H^+ velocity at the top, O^+ versus He^+ velocity in the middle, and He^+ versus H^+ velocity at the bottom. The right panels are O^+/H^+ (top), O^+/He^+ (middle), He^+/H^+ (bottom) velocity ratio histograms. The solid lines represent the average parallel velocity ratios.

Figure 21. The left panels are the O^+ versus H^+ number flux on the top, He^+ versus O^+ number flux in the middle, and He^+ versus H^+ number flux at the bottom. The right panels are O^+/H^+ (top), He^+/O^+ (middle), He^+/H^+ (bottom) number flux ratio histograms. The solid lines represent the average number flux ratios.

Figure 22. The histograms of the occurrence frequency versus the parallel/perpendicular temperature ratios for H^+ (top-right) and O^+ (bottom-right) are shown in the right two panels at $8 R_E$ altitude. Plots on the left are the parallel temperature versus perpendicular temperature for H^+ (top-left) and O^+ (bottom-left). The solid lines represent the average values.

Figure 23. The histograms of the occurrence frequency versus the O^+/H^+ parallel (top-right) and perpendicular temperature (bottom-right) ratios are shown in the right two panels at $8 R_E$ altitude. Plots on the left two panels are the O^+ versus H^+ temperature for both parallel (top-left) and perpendicular component (bottom-left). The solid lines represent the average values.

Figure 24. The parallel Mach number histograms for H^+ (top) and O^+ (bottom) at $8 R_E$ altitude. The solid lines represent the average Mach numbers.

Figure 25. The O^+ (a) and H^+ (b) bulk parameters, including density (top), velocity (middle), and parallel temperature (bottom), versus the X_{SM} at POLAR apogee. The open triangle symbols are the average values over the interval of $0.4 R_E$.

Figure 26. H^+ density versus O^+ density in log scale at POLAR perigee. The large solid circles with solid line are the average values. The straight line is the linear least-square fit in log scale with the correlation coefficient = 0.8.

Figure 27. Comparison of survey parameter ranges with photoelectron-driven polar wind (solar minimum conditions) from 120 km to $9 R_E$ altitude [Su *et al.*, 1998]. (left) Electric potential. The solid line represents the potential with photoelectron effects and the long-dashed line represents the base-line polar

wind case. (middle) Ion bulk velocities and (right) densities. The solid and dot-dashed lines represent the O^+ and H^+ profiles for photoelectron-driven polar wind case, while the long-dashed and short-dashed lines for the base-line polar wind case (no photoelectron effects included). The horizontal solid and dashed lines present the range of TIDE observed polar wind characteristics for H^+ and O^+ at 5000 km and $8 R_E$ altitude.

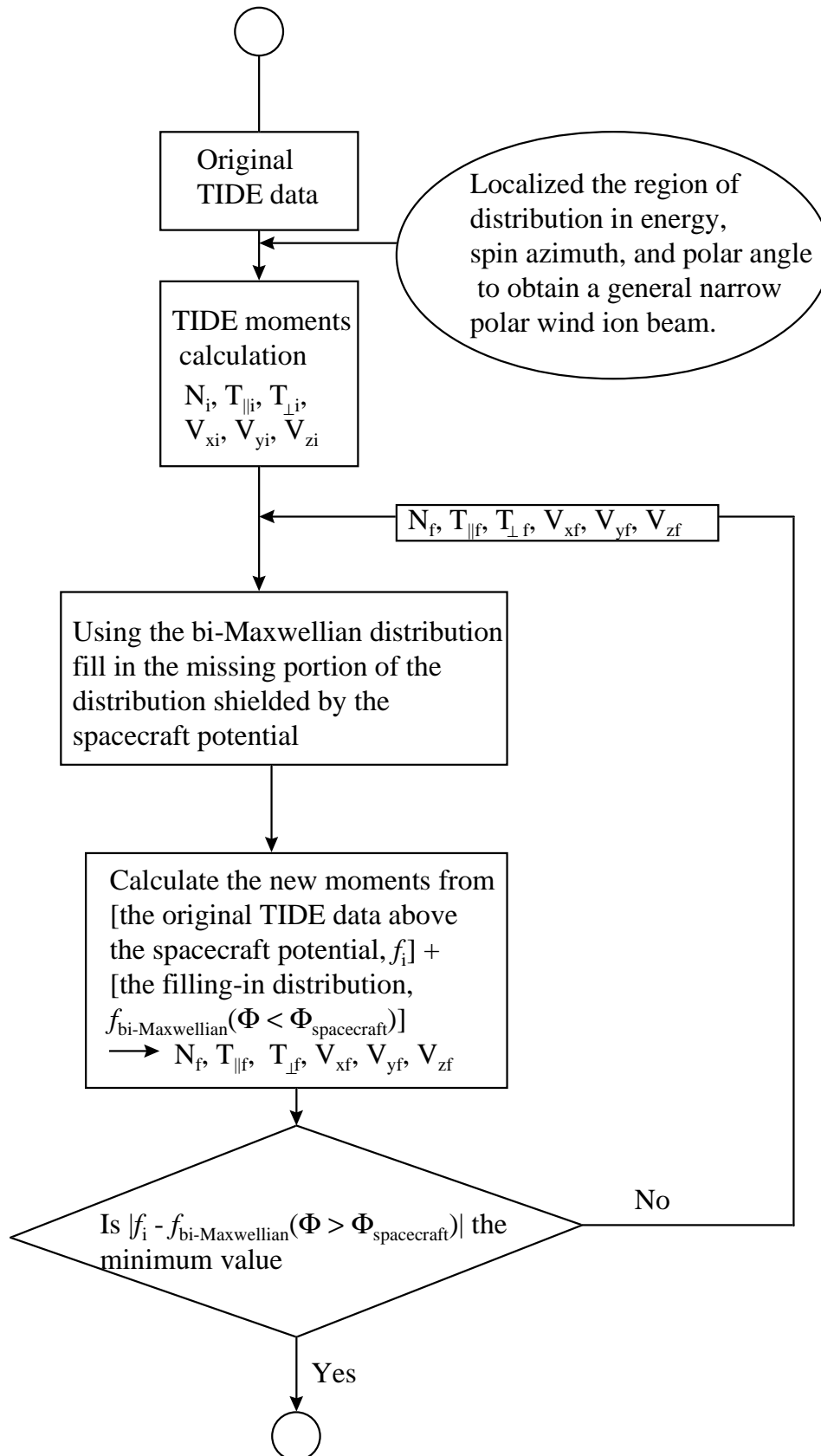


Fig 3